Scanning Error Compensation in Ground-Based ArcSAR Monitoring

Yunkai Deng, Hanpu Zhou, Weiming Tian, Xin Xie, Wenyu Li, and Cheng Hu

***Abstract*—Ground-based arc-scanning synthetic aperture radar (GB-ArcSAR) can perform 360° scanning and has a large field of view. Based on the differential interferometry technique, GB-ArcSAR can be utilized to measure the surface deformation. However, affected by the rotating motion, rescanning angle error and rotation center offset during repeated scanning could occur. Through theoretical analysis, this article proves that the rescanning angle error has nearly no effect on the interferometric phase and can be negligible. The phase error caused by the rotation center offset can be built as a linear multiparameter model based on the multivariate Taylor expansion. Simulations are made to analyze the effect of the rotation center offset. A compensation method based on permanent scatterer technology is proposed, by using the least squares method, which jointly compensates the rotation center offset error and the atmospheric phase disturbance error. The compensation performance of the proposed method is validated in different scenarios, which can effectively improve the accuracy of deformation measurement.**

***Index Terms*—Ground-based arc-scanning synthetic aperture radar (Gb-ArcSAR), multiparameter model, permanent scatterer (PS), rotation center offset error.**

I. Introduction

DEFORMATION monitoring is an important basis for predicting and warning landslide disasters, frozen soil pavement, construction, and other fields [1]. Synthetic aperture radar (SAR) has a wide range of applications in deformation monitoring, with the advantages of being all-time, all-weather, and large-scale [2], [3], which is typically based on differential interferometric technology [4]. Spaceborne SAR has a large coverage range, but its measurement period is limited by the revisit period, and the observation perspective is not flexible enough [5]. Ground-based SAR (GB-SAR) works on a ground platform and can adjust its placement according to the observation scene. It has a short monitoring period and performs near real-time deformation monitoring [6], [7]. The deformation measurement accuracy of GB-SAR can reach millimeter to submillimeter level [8].

GB-SAR can be divided into three types: line-scanning GB-SAR, ground-based arc-scanning SAR (GB-ArcSAR), and ground-based multiple-input multiple-output (GB-MIMO) radar, according to different synthetic aperture modes [1]. The transmitting and receiving antennas of line-scanning GB-SAR move along the slide track to form a large synthetic aperture [9], and the GB-MIMO radar uses multiple transmitting and receiving antennas to form a special array [10]. Both of them can only observe at a certain angle range covered by the antenna beam. GB-ArcSAR can obtain a 360° view through rotation and has a much larger monitoring coverage than the other two types [11].

However, in practice, it is difficult to avoid the rotation errors of a GB-ArcSAR system by other means. Typical rotation errors include the angle deviation when rescanning and a slight offset of the rotation center. Both cases would cause error phase components in the differential interferometry measurement. In the long-term monitoring, if the error phase components cannot be compensated with high accuracy, the deformation measurement accuracy will be affected. The rescanning angle error and the rotation center offset error are both very small when adopting a high-precision turntable, but they cannot be ignored in order to ensure the deformation measurement accuracy on the submillimeter level. However, it is difficult to measure the rotation errors directly by other means in practice.

In GB-ArcSAR measurement, errors caused by the rotation arm are commonly omitted. The main error source is the atmospheric phase disturbance, and it can be compensated by building a multiparameter model using the unwrapping phase of permanent scatterer (PS) [12]. As for the rescanning error, there are some related research works on linear scanning GB-SAR. The first type considers the mechanical reset error of the sliding track. When the radar cannot accurately move from the starting to the end of the sliding track every time during repeating measurements, small reset errors due to the imperfect repeatability of synthetic aperture scans on the submillimeter or millimeter scale can occur and it can be compensated by building a simplified model related with the azimuth angle [13]. The second type considers the repositioning error in GB-SAR discontinuous monitoring, since the radar system needs to be

Manuscript received 8 January 2024; revised 3 April 2024; accepted 26 April 2024. Date of publication 9 May 2024; date of current version 23 May 2024. This work was supported in part by the National Natural Science Foundation of China under Grant 62101036, in part by Foundation of China State Construction Engineering Corporation under Grant CSCEC-2022-Z-4, and in part by Beijing Institute of Technology Research Fund Program for Young Scholars. *(Corresponding author: Weiming Tian.)*

Yunkai Deng is with the Radar Technology Research Institute, Beijing Institute of Technology, Beijing 100081, China (e-mail: yunkai_bit@foxmail.com).

Hanpu Zhou, Xin Xie, and Wenyu Li are with the Key Laboratory of Electronic and Information Technology in Satellite Navigation, Beijing Institute of Technology Ministry of Education, Beijing 100081, China (e-mail: zhouhp@bit.edu.cn; 3120215409@bit.edu.cn; l_wy9746@163.com).

Weiming Tian is with the Beijing Institute of Technology Chongqing Innovation Center, Beijing Institute of Technology, Chongqing 401120, China (e-mail: tianwei6779@163.com).

Cheng Hu is with the Advanced Technology Research Institute, Beijing Institute of Technology, Jinan 250300, China (e-mail: cchchb@163.com).

Digital Object Identifier 10.1109/JSTARS.2024.3398817

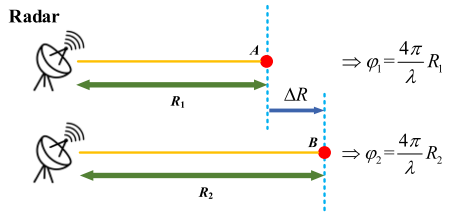

Fig. 1. Schematic diagram of differential interferometry.

installed and disassembled repeatedly [14], [15]. For continuous measurement of GB-ArcSAR, there is also a rotational center offset error. When the radar rotates in the azimuth direction to form an arc-shaped synthetic aperture, it may be affected by external interference and other factors, resulting in a slight deviation of the rotation circle. At the present stage, no relevant research works on how to model and compensate for the rotation errors of GB-ArcSAR have been reported.

This article analyses the effect of the rescanning angle error and the rotation center offset error on the interferometric phase. Theoretical analysis proves that the rescanning angle error can be negligible. Then, this article analyzes the rotation center offset error based on the GB-ArcSAR imaging geometry, and obtains the functional relationship between the error model and the three-dimensional (3-D) coordinates of the targets based on the multivariate Taylor expansion. This article proposes a differential interferometric measurement error compensation method based on the PS technology. By using the least squares method, this article estimates the error phase and jointly compensates for the rotation center offset error and the atmospheric disturbance phase. Coner reflector experiments and real-scene monitoring experiments were conducted on the GB-ArcSAR system. The effectiveness of the proposed method was verified by comparing and analyzing the results of only atmospheric phase compensation and joint compensation.

II. Rotation Error in GB-ArcSAR

GB-ArcSAR utilizes the differential interferometry technique to measure the surface deformations [16]. The basic principle is shown in Fig. 1. If the position of a target changes during two acquisitions, under ideal conditions, its phase change can be expressed as

$$\Delta\varphi = \varphi_1 - \varphi_2 = 4\pi\frac{R_1 - R_2}{\lambda} = \frac{4\pi}{\lambda}\Delta R \tag{1}$$

where R_1 is the initial distance between the target and the radar, R_2 is its changed distance, λ is the radar wavelength, and $\Delta\varphi$ is the deformation phase without considering the phase wrapping. The deformation ΔR can be estimated based on (1).

GB-ArcSAR acquires a large synthetic aperture by rotating the antennas in the horizontal plane. In the long-term repeated mechanical scanning, two types of rotation errors, including the rescanning angle error and the rotation center offset error, are inevitable. The rescanning angle error is the angular reset error when the antennas rotate from or return to the starting position, resulting in an overall angle deviation in the azimuth direction during repeated measurements. The rotation center offset error is caused by the instability of the rotation platform itself, resulting in a phase error due to the range variation between the target and the radar system.

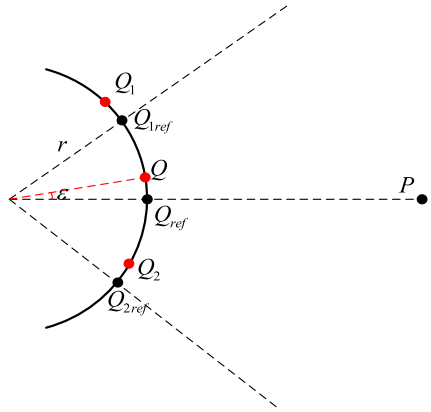

Fig. 2. Rescanning error diagram.

A. Rescanning Angle Error

Fig. 2 shows a schematic diagram of the rescanning angle error in the range-azimuth plane. O is the rotation center and its coordinate is (00,0). P is a target with the coordinate of (0, R, h). Its coherent integral arc is $Q_{1\text{ref}}Q_{2\text{ref}}$. Q_{ref} is the middle point of the arc, and its coordinate is (0, r,0). Considering the phenomenon of azimuth translation invariance in GB-ArcSAR imaging, the azimuth coordinates of the target P and the arc center Q_{ref} are both set to be zero. Their distance $|PQ_{\text{ref}}|$can be expressed as

$$|\text{PQ}_{\text{ref}}| = \sqrt{(R-r)^2 + h^2}. \tag{2}$$

When there is a rescanning angle error ε, assume that the coherent integral arc of P changes to $\overset{\frown}{Q_1Q_2}$, and Q is the middle point of the arc. The distance $|PQ|$ between P and Q is

$$|PQ| = \sqrt{r^2 + R^2 + h^2 - 2rR\cos\varepsilon}. \tag{3}$$

The phase component caused by the rescanning angle error can be expressed as

$$\begin{aligned}\varphi_{\text{re}} &= \frac{4\pi}{\lambda}\left(|PQ_{\text{ref}}| - |PQ|\right)\\ &= \frac{4\pi}{\lambda}\left(\sqrt{(R-r)^2 + h^2} - \sqrt{r^2 + R^2 + h^2 - 2rR\cos\varepsilon}\right)\\ &= \frac{4\pi}{\lambda}\left[-\frac{Rr\varepsilon^2}{\sqrt{r^2 + R^2 + h^2 - 2rR\cos\varepsilon}} + O(\varepsilon^3)\right].\end{aligned} \tag{4}$$

To quantitively analyze the value of φ_{re}, a numerical simulation is made, using rotation radius $r = 1.177$ m and wavelength $\lambda = 0.0185$ m. Fig. 3(a) shows the change of $\varphi_{re}$with rescanning angle error and range when the height is 10 m. Fig. 3(b) shows the change of $\varphi_{re}$with reset angle error and height when the range is 300 m. The error phase value of both is just on the order

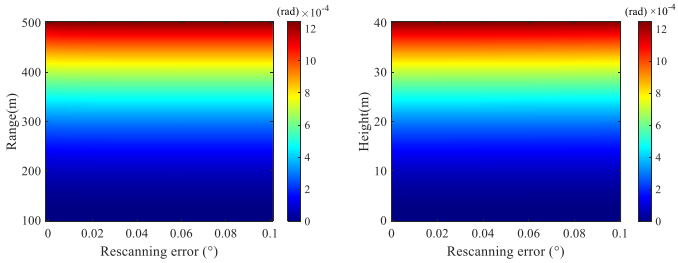

Fig. 3. Phase component cause by the rescanning angle error. (a) Variation of error phase with range and reset error. (b) Variation of error phase with height and reset error.

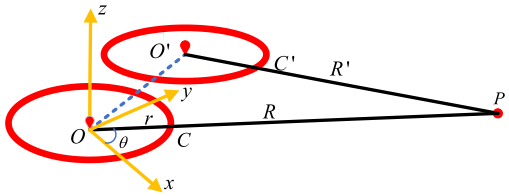

Fig. 4. Geometry diagram of the rotation center offset.

of 10^{-3} rad. Therefore, for a rotating platform with an angle repetition accuracy better than 0.1°, the rescanning angle error can be negligible.

B. Rotation Center Offset Error

Fig. 4 shows the geometric relationship before and after the rotation center offset, where x is the azimuth axis, y is the range axis, and z is the height axis [17]. P denotes the target, and its coordinate is (x_p, y_p, z_p). O is the rotation center, and its coordinate is (00,0). C is the position of the antenna, which is located at the end of the rotation arm. r is the rotation radius.

The azimuth angle of P is $\theta = \tan^{-1}(x_p/y_p)$. Then the range R between P and C can be expressed as

$$R = \sqrt{(x_p - r\cos\theta)^2 + (y_p - r\sin\theta)^2 + z_p^2}. \tag{5}$$

O' is the rotation center after offset, and its coordinate is assumed to be $(\varepsilon_x, \varepsilon_y, \varepsilon_z)$. The azimuth angle θ' of the target P is

$$\theta' = \tan^{-1}\left((x_p - \varepsilon_x)/(y_p - \varepsilon_y)\right). \tag{6}$$

Since the offsets $\varepsilon_x$andε_y are both small and their values are typically on the submillimeter or millimeter level, which are much smaller than the ground range, θ' can be approximated as θ.

The range R' between P and C'after the rotation center offset can be expressed as

$$R'(\varepsilon_x, \varepsilon_y, \varepsilon_z) = \sqrt{(x_p - r\cos\theta - \varepsilon_x)^2 + (y_p - r\sin\theta - \varepsilon_y)^2 + (z_p - \varepsilon_z)^2}. \tag{7}$$

Performing a multivariate Taylor series expansion on $R'(\varepsilon_x, \varepsilon_y, \varepsilon_z)$ at (00,0), we can obtain

$$\begin{aligned}
R'(\varepsilon_x, \varepsilon_y, \varepsilon_z) &\approx R'|_{(0,0,0)} \\
&+ \begin{bmatrix} \frac{\partial R'}{\partial \varepsilon_x}\Big|_{(0,0,0)} & \frac{\partial R'}{\partial \varepsilon_y}\Big|_{(0,0,0)} & \frac{\partial R'}{\partial \varepsilon_z}\Big|_{(0,0,0)} \end{bmatrix} \begin{bmatrix} \varepsilon_x \\ \varepsilon_y \\ \varepsilon_z \end{bmatrix} \\
&+ \frac{1}{2}\begin{bmatrix} \varepsilon_x & \varepsilon_y & \varepsilon_z \end{bmatrix} \\
&\begin{bmatrix} \frac{\partial^2 R'}{\partial \varepsilon_x^2}\Big|_{(0,0,0)} & \frac{\partial^2 R'}{\partial \varepsilon_x \partial \varepsilon_y}\Big|_{(0,0,0)} & \frac{\partial^2 R'}{\partial \varepsilon_x \partial \varepsilon_z}\Big|_{(0,0,0)} \\ \frac{\partial^2 R'}{\partial \varepsilon_x \partial \varepsilon_y}\Big|_{(0,0,0)} & \frac{\partial^2 R'}{\partial \varepsilon_y^2}\Big|_{(0,0,0)} & \frac{\partial^2 R'}{\partial \varepsilon_y \partial \varepsilon_z}\Big|_{(0,0,0)} \\ \frac{\partial^2 R'}{\partial \varepsilon_x \partial \varepsilon_z}\Big|_{(0,0,0)} & \frac{\partial^2 R'}{\partial \varepsilon_y \partial \varepsilon_z}\Big|_{(0,0,0)} & \frac{\partial^2 R'}{\partial \varepsilon_z^2}\Big|_{(0,0,0)} \end{bmatrix} \begin{bmatrix} \varepsilon_x \\ \varepsilon_y \\ \varepsilon_z \end{bmatrix} \\
&= R - \frac{x_p - r\cos\theta}{R}\varepsilon_x - \frac{y_p - r\sin\theta}{R}\varepsilon_y - \frac{z_p}{R}\varepsilon_z \\
&+ \frac{\left(R_1^2 - (x_p - r\cos\theta)^2\right)}{2R^3}\varepsilon_x^2 + \frac{\left(R_1^2 - (y_p - r\sin\theta)^2\right)}{2R^3}\varepsilon_y^2 \\
&+ \frac{\left(R_1^2 - z_p^2\right)}{2R^3}\varepsilon_z^2 \\
&- \frac{(x_p - r\cos\theta)(y_p - r\sin\theta)}{R^3}\varepsilon_x\varepsilon_y - \frac{(x_p - r\cos\theta)z_p}{R^3}\varepsilon_x\varepsilon_z \\
&- \frac{(y_p - r\sin\theta)z_p}{R^3}\varepsilon_y\varepsilon_z.
\end{aligned} \tag{8}$$

In (8), $R'|_{(0,0,0)} = R$.

Therefore, the range variation ΔR is

$$\begin{aligned}
\Delta R = R'(\varepsilon_x, \varepsilon_y, \varepsilon_z) - R &= -\frac{x_p - r\cos\theta}{R}\varepsilon_x \\
&- \frac{y_p - r\sin\theta}{R}\varepsilon_y - \frac{z_p}{R}\varepsilon_z \\
&+ \frac{\left(R^2 - (x_p - r\cos\theta)^2\right)}{2R^3}\varepsilon_x^2 \\
&+ \frac{\left(R^2 - (y_p - r\sin\theta)^2\right)}{2R^3}\varepsilon_y^2 + \frac{\left(R^2 - z_p^2\right)}{2R^3}\varepsilon_z^2 \\
&- \frac{(x_p - r\cos\theta)(y_p - r\sin\theta)}{R^3}\varepsilon_x\varepsilon_y \\
&- \frac{(x_p - r\cos\theta)z_p}{R^3}\varepsilon_x\varepsilon_z - \frac{(y_p - r\sin\theta)z_p}{R^3}\varepsilon_y\varepsilon_z.
\end{aligned} \tag{9}$$

Since the rotation center offset is much smaller than the slant range, the quadratic term is much smaller than the linear one, and it can be ignored. Therefore, the error phase caused by the rotation center offset can be expressed as

$$\Delta\varphi_{\text{geom}} = -\frac{4\pi}{\lambda}\left(\frac{x_p - r\cos\theta}{R}\varepsilon_x + \frac{y_p - r\sin\theta}{R}\varepsilon_y + \frac{z_p}{R}\varepsilon_z\right). \tag{10}$$

To illustrate the effects of the rotation center offset error, the interferometric phase under different types of rotation center offsets is simulated with wavelength $\lambda = 0.0185$ m. As shown

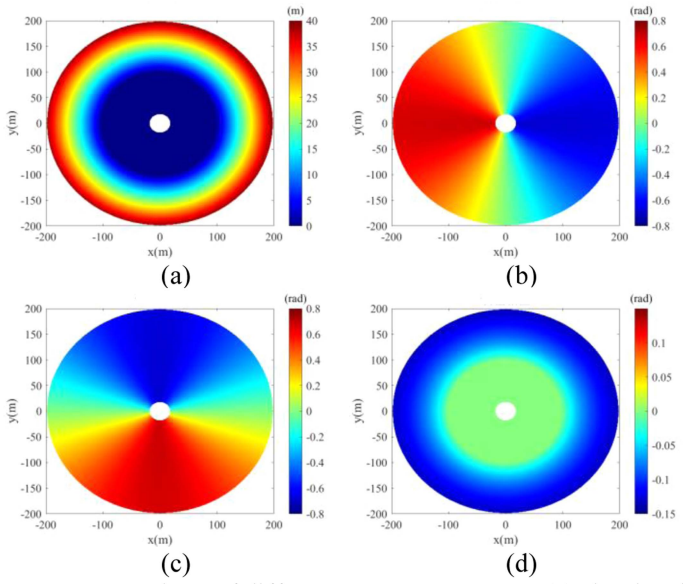

Fig. 5. Error phase of different error components. (a) Simulated terrain. (b) $\varepsilon_x = 1\,\text{mm}, \varepsilon_y = 0, \varepsilon_z = 0$. (c) $\varepsilon_x = 0, \varepsilon_y = 1\,\text{mm}, \varepsilon_z = 0$. (d) $\varepsilon_x = 0, \varepsilon_y = 0, \varepsilon_z = 1\,\text{mm}$.

in Fig. 5(a), a circular 3-D terrain composed of a flat land and a slope is constructed. Fig. 5(b)–(d) shows the error phase diagram under different offsets. When there is only rotation offset error component in the azimuth direction with $\varepsilon_{\text{x}} = 1$ mm, the error phase $\Delta\varphi_{\text{geom}}$ changes with the azimuth angle. When the rotation error is set as $\varepsilon_y = 1$ mm, the error phase $\Delta\varphi_{\text{geom}}$ also changes with the azimuth angle. When there is only vertical error component $\varepsilon_z = 1$ mm, the error phase $\Delta\varphi_{\text{geom}}$ in the flat area is 0, but in the slope area, the error phase gradually increases as the slope height increases. Therefore, the error phase introduced by ε_x and ε_y changes with the azimuth angle and is almost unaffected by the height, and the error phase introduced by ε_z is only affected by the height.

III. Error Compensation Based on PS Technology

Interferometric phase quality is the most crucial element that determines the accuracy of GB-ArcSAR deformation measurement. To select pixels suitable for phase analysis, the PS technique is commonly applied. The PS method estimates pixels' phase stability with the amplitude dispersion index (ADI) [18]. The interferometric phase of a PS after phase unwrapping can be modeled as

$$\Delta\varphi_{\text{PS}} = \Delta\varphi_{\text{defo}} + \Delta\varphi_{\text{atmo}} + \Delta\varphi_{\text{geom}} + \Delta\varphi_{\text{noise}} \tag{11}$$

where $\Delta\varphi_{\text{defo}}$ is the deformation phase, $\Delta\varphi_{\text{atmo}}$ is the atmospheric disturbance phase, $\Delta\varphi_{\text{geom}}$ is the rotation error phase, and $\Delta\varphi_{\text{noise}}$ is the phase error caused by thermal noise.

The phase error caused by the rotation center offset is modeled as

$$\Delta\varphi_{\text{geom}} = \frac{4\pi}{\lambda}\left(A_1\frac{x_p - r\cos\theta}{R} + A_2\frac{y_p - r\sin\theta}{R} + A_3\frac{z_p}{R}\right). \tag{12}$$

For the atmospheric disturbance phase $\Delta\varphi_{\text{atmo}}$, when the atmosphere in the scene is uniformly distributed, $\Delta\varphi_{\text{atmo}}$ can be constructed into a model that changes linearly with the slant range

$$\Delta\varphi_{\text{atmo}} = \frac{4\pi}{\lambda}\left(B_1 R + B_2\right) \tag{13}$$

where B_1 is the linear coefficient and B_2 is a constant.

When the atmosphere is nonuniformly distributed, the atmospheric phase shows complex spatial variability and some complicated parametrical models are utilized to simulate $\Delta\varphi_{\text{atmo}}$. When considering that the refractivity distribution may exhibit horizontal inhomogeneity, a new interferometric signal model to jointly estimate the deformation velocity and residual atmospheric disturbance phase is proposed [19]. When there are terrain changes in the scene, the atmospheric refraction will change with the scene height. Then the atmospheric phase component can be constructed as a range-height model [20]

$$\Delta\varphi_{\text{atmo}} = \frac{4\pi}{\lambda}\left(C_1 R + C_2 R z_p + C_3\right) \tag{14}$$

where C_1 is the linear coefficient, C_2 is the "range-height" coefficient, and C_3 is a constant.

Taking the atmospheric disturbance phase in (14) as an example, the interferometric phase $\Delta\varphi_{PS}$ of a PS without deformation can be expressed as

$$\Delta\varphi_{PS} = \frac{4\pi}{\lambda}\left(A_1\frac{x_p - r\cos\theta}{R} + A_2\frac{y_p - r\sin\theta}{R} + A_3\frac{z_p}{R} + C_1 R + C_2 R z_p + C_3 + e\right) \tag{15}$$

where $[A_1, A_2, A_3, C_1, C_2, C_3]$ is the parameter to be estimated, and e is the random noise phase.

A system of equations can be built as follows:

$$\Delta\Phi = X\beta + \text{E} \tag{16}$$

where

$$\Delta\Phi = \begin{bmatrix}\Delta\varphi_1\\ \Delta\varphi_2\\ \vdots\\ \Delta\varphi_N\end{bmatrix} \quad X = \frac{4\pi}{\lambda}$$

$$\begin{bmatrix} \frac{x_1 - r\cos\theta_1}{R_1} & \frac{y_1 - r\sin\theta_1}{R_1} & \frac{z_1}{R_1} & R_1 & R_1 z_1 & 1\\ \frac{x_2 - r\cos\theta_2}{R_2} & \frac{y_2 - r\sin\theta_2}{R_2} & \frac{z_2}{R_2} & R_2 & R_2 z_2 & 1\\ \vdots & \vdots & \vdots & \vdots & \vdots & \vdots\\ \frac{x_N - r\cos\theta_N}{R_N} & \frac{y_N - r\sin\theta_N}{R_N} & \frac{z_N}{R_N} & R_N & R_N z_N & 1 \end{bmatrix}$$

$$\beta = \begin{bmatrix}A_1\\ A_2\\ A_3\\ C_1\\ C_2\\ C_3\end{bmatrix} \quad \text{E} = \frac{4\pi}{\lambda}\begin{bmatrix}e_1\\ e_2\\ \vdots\\ e_N\end{bmatrix} \tag{17}$$

where $\Delta\Phi$ is an $N \times 1$-dimensional vector composed of the interferometric phases of N PSs. X is a $N \times 6$ matrix depending

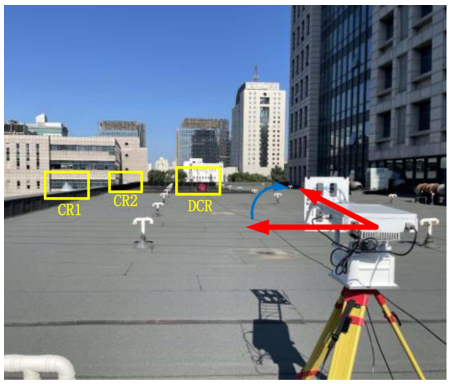

Fig. 6. System and experimental scene.

TABLE I
SYSTEM PARAMETERS

Parameter	Value	Parameter	Value
Signal form	FMCW (Frequency Modulated Continuous Wave)	Signal duration	0.5 ms
		Sampling rate	20 MHz
Carrier frequency	16.2 GHz	Rotation arm length	1.18 m
Bandwidth	800 MHz	Beamwidth	40°

on the 3-D coordinates, slant range, and azimuth angle of the PSs. β is a 6×1 vector composed of the parameters to be estimated, and E is an $N \times 1$ vector composed of random errors.

According to the least squares estimation algorithm, the parameter vector β is estimated, and we can obtain

$$\hat{\beta} = \left(X^T X\right)^{-1} X^T \Delta\Phi \tag{18}$$

where ^{T} is the matrix transpose.

Hence, the estimated error component $\Delta\hat{\Phi}$ of the PSs is

$$\Delta\hat{\Phi} = X\hat{\beta}. \tag{19}$$

Finally, $\Delta\hat{\Phi}$ is subtracted from $\Delta\Phi$ to achieve error phase compensation. In actual processing, there are PSs with deformations that will affect the estimation accuracy. In order to improve the measurement accuracy, unreliable PSs can be filtered out according to (20) [21]. The typical value of φ_T is within 0.1–0.2 rad, and then a secondary estimation compensation is performed

$$\left|\Delta\Phi - \Delta\hat{\Phi}\right| < \varphi_T. \tag{20}$$

IV. EXPERIMENTAL RESULTS

A. Corner Reflector (CR) Experiment

Fig. 6 shows the GB-ArcSAR system independently developed by the Radar Research Laboratory of Beijing Institute of Technology. Table I shows the system parameters. The right side of the scene is a building, the other three sides are low walls, and there are some evenly distributed plastic pipes in the middle. During the experiment, two CRs were placed on the left side and a displacement CR (DCR) was placed in the middle of the scene.

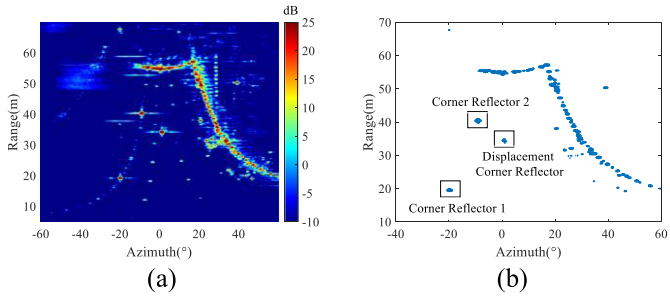

Fig. 7. (a) SNR image. (b) PS selection result.

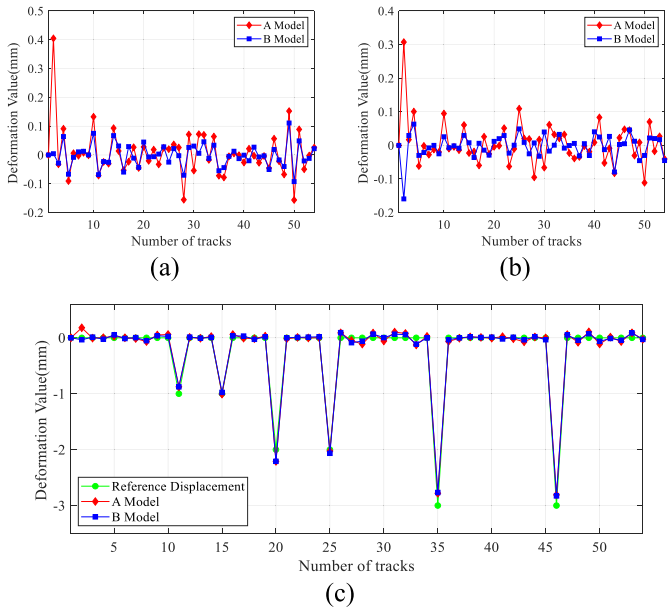

Fig. 8. Deformation curves of three CRs. (a) CR1. (b)CR2. (c) DCR.

The radar system works in a fan scan mode. The scanning angle range is -90°to 90°, and the rotation speed is 5°/s.

The collection started at 16:20 on July 13, 2022, and ended at 17:08. A total of 54 images were collected. The DCR was set to move 1 mm on the 11th and 15th image, 2 mm on the 20th and 25th images, and 3 mm on the 35th and 46th images. Fig. 7(a) is the signal-to-noise ratio (SNR) map. An amplitude dispersion threshold of 0.1 and an SNR threshold of 15 dB were used for the PS selection, and a total of 2083 PSs were selected. Fig. 7(b) shows the PS selection result and marks the positions of the CRs.

Two models are respectively utilized to compensate for the error phase components. A model is the slant range-height model in (13), which is only utilized to compensate the atmospheric disturbance phase, and B model is the joint compensation model in (15).

Fig. 8 shows the time series deformation curves of different CRs after compensation using models A and B. The two fixed CRs are used as reference. It can be noted that the deformation value fluctuations are smaller when using B model. For the

TABLE II
STANDARD DEVIATION OF THE DEFORMATION MEASUREMENT ERRORS AFTER COMPENSATION WITH DIFFERENT MODELS

	Standard deviation (mm)		
	CR1	CR2	DCR
Uncompensated	0.1341	0.1263	0.1250
Model A	0.0849	0.0547	0.0790
Model B	0.0449	0.0368	0.0703

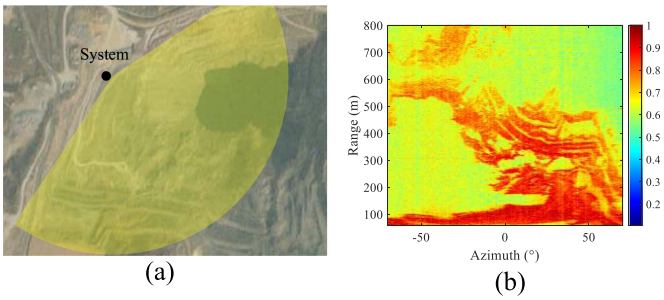

Fig. 9. (a) Experimental scene. (b) SAR image.

DCR, its deformation values are consistent with the preset displacement.

Table II shows the standard deviation of the deformation error when using different compensation models. The deformation measurement accuracy after compensation by models A and B has been greatly improved, but model B has a better improvement performance and it reaches submillimeter accuracy. This result verifies the accuracy of the model proposed in this article.

B. Open Pit Mine Experiment

Beijing Shouyun Iron Mine ($N\,40°22'51''$, $E\,117°1'54''$) is an open-pit mine with sparse vegetation. The experimental scene is shown in Fig. 9(a). The sector denotes the location of the radar system. The system parameters are shown in Table I. The collection started at 12:58 on March 28, 2023, and ended at 15:08, which lasted for 2 h and 10 min. A total of 113 images were collected. Fig. 9(b) shows the SAR image in polar coordinates. The scene in the lower left corner is a puddle, and the hillside texture on the right is clear.

Set the amplitude dispersion threshold to 0.1, and the SNR threshold to 10 dB. A total of 41 108 PSs are selected. The interferometric phase map of the PSs acquired with the 96th and 97th images is shown in Fig. 10.

Interferometry processing was performed on two adjacent SAR images, and a total of 112 interferometric phase images were obtained. Using A model to estimate the error phase of the PSs, the scatter diagram $\mathrm{SD}^{(k)}_{\mathrm{A-R}}$ (SD, Scattered Diagram) of the interferometric phase distribution along with the slant range is shown in Fig. 11(a) and $\mathrm{SD}^{(k)}_{\mathrm{A-A}}$ along with the azimuth angles is shown in Fig. 11(b), where $^{(k)}$ is the kth interferometric phase map. It can be noted that using only the atmospheric phase model, the distribution of the model estimation results and the actual interferometric phase cannot accurately match. Fig. 11(c) and (d) shows the scatter diagrams $\mathrm{SD}^{(97)}_{\mathrm{B-R}}$ and $\mathrm{SD}^{(97)}_{\mathrm{B-A}}$ estimated

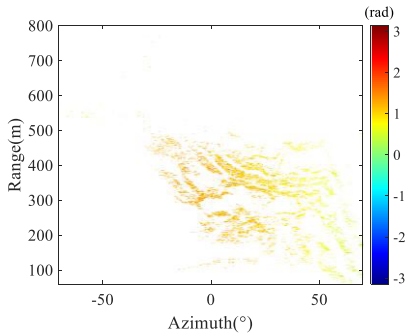

Fig. 10. Interferometric phase map of the selected PSs after phase unwrapping.

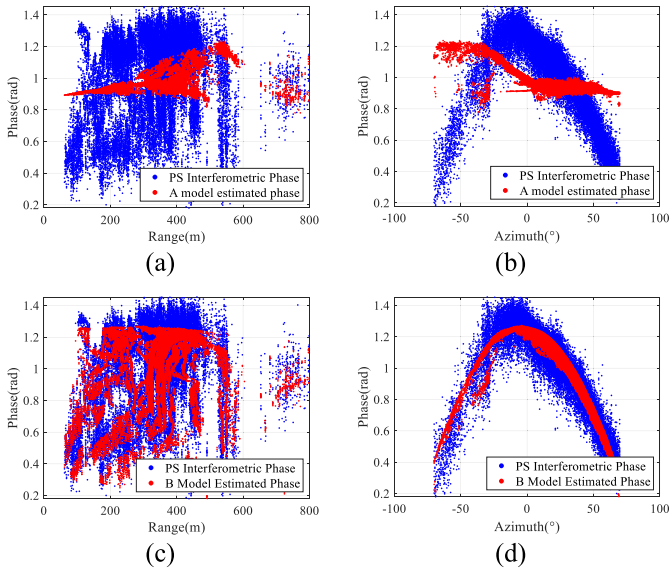

Fig. 11. Estimation results of model A and B. (a) $\mathrm{SD}^{(97)}_{\mathrm{A-R}}$. (b) $\mathrm{SD}^{(97)}_{\mathrm{A-A}}$. (c) $\mathrm{SD}^{(97)}_{\mathrm{B-R}}$. (d) $\mathrm{SD}^{(97)}_{\mathrm{B-A}}$.

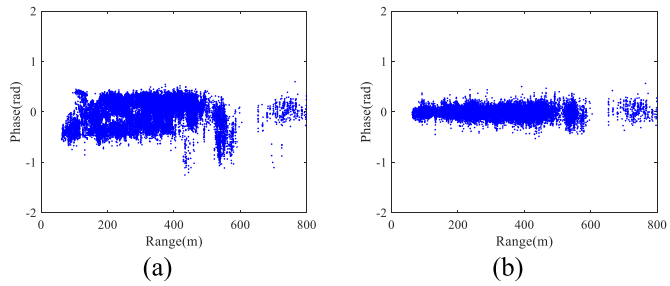

Fig. 12. Scatter diagram of compensated phase. (a) Model A, 97th image. (b) Model B, 97th image.

by the model B respectively. It can be seen from Fig. 11(c) and (d) that when the rotation center offset error and atmospheric phase are jointly compensated, the distribution of the estimated results is consistent with that of the interferometric phase.

Fig. 12 shows the residual error phase diagram of the 97th interferometric phase map after compensation using the A and B models. The residual error phase refers to the difference between

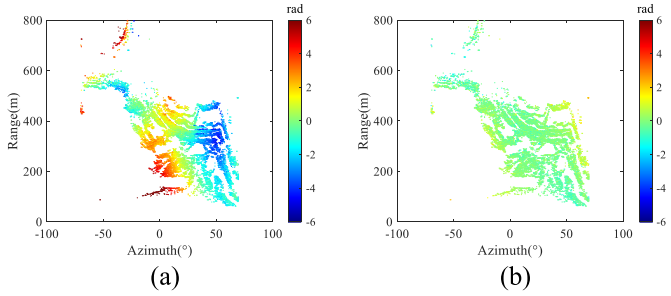

Fig. 13. Accumulated deformation phase after compensation. (a) A model. (b) B Model.

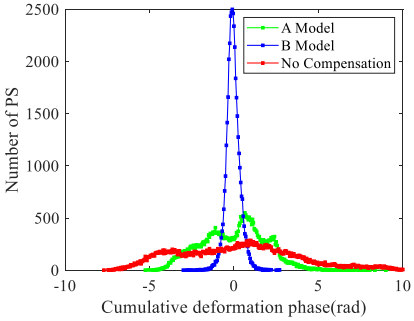

Fig. 14. Cumulative deformation phase distribution curves of different models.

the phase estimated by the models and the real unwrapped phase of PSs. When only the range-height model is used, the compensation effect is poor, and large residuals still exist after compensation. When using the A and B models, the compensated phase standard deviations of the 97th map are 0.2395 rad and 0.0763 rad respectively. The compensation performance with the B model is better.

Fig. 13 shows the cumulative deformation phase maps with the two models. It can be seen that when the A model is used for compensation, a large number of PSs still retain phase components that change along the azimuth. Model B estimates and compensates for the rotation center offset error, and the residual phase is basically distributed around 0 rad. The distribution of the cumulative deformation phase is shown in Fig. 14. We can conclude that a better compensation performance could be achieved using model B, which jointly compensates the phase error.

C. Foundation Pit Monitoring Experiment

A differential interferometry experiment was conducted in Pinggu district, Beijing, on May 10, 2023. The system parameters are shown in Table I. The collection started at 12:19 and ended at 15:54. A total of 185 images were collected, which lasted for 3 h and 35 min. Fig. 15(a) shows the scene of the foundation pit, and Fig. 15(b) shows the SAR image in polar coordinates.

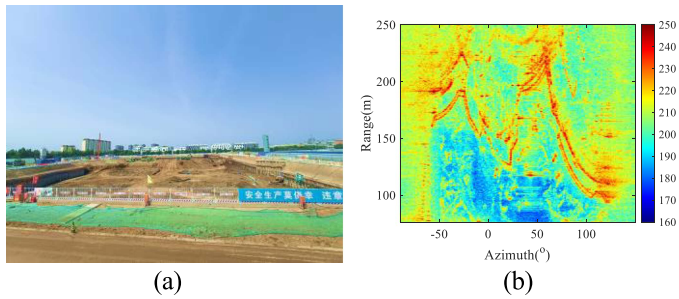

Fig. 15. (a) Experimental scene. (b) SAR image.

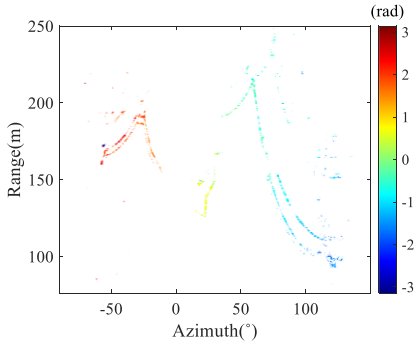

Fig. 16. PS selection result.

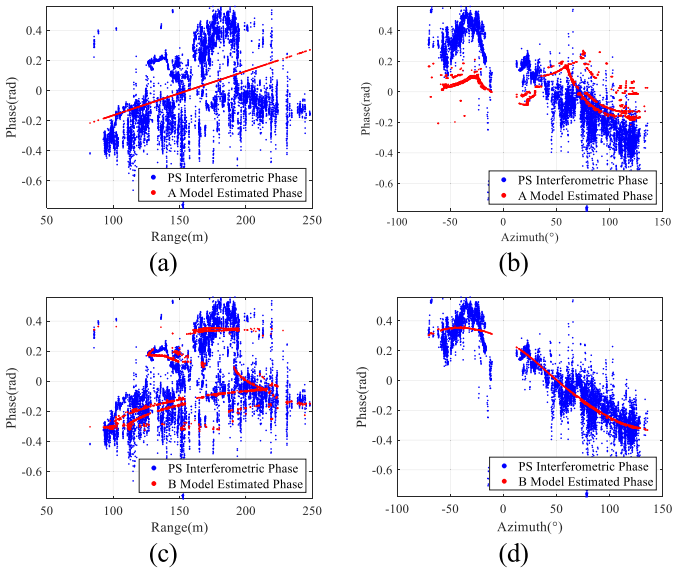

Fig. 17. Phase estimation results with the A and B models. (a) $SD^{(2)}_{A-R}$. (b) $SD^{(2)}_{A-A}$. (c) $SD^{(2)}_{B-R}$. (d) $SD^{(2)}_{B-A}$.

Using all the 185 images, 12 988 PSs were selected by using the amplitude deviation threshold of 0.15 and the SNR threshold of 25 dB. Fig. 16 shows the interferometric phase of the PSs.

When using the A model, the scatter plot $SD^{(2)}_{A-R}$ and $SD^{(2)}_{A-A}$ are shown in Fig. 17(a) and (b). When using the B model, $SD^{(2)}_{B-R}$ and $SD^{(2)}_{B-A}$ are shown in Fig. 17(c) and (d). It can

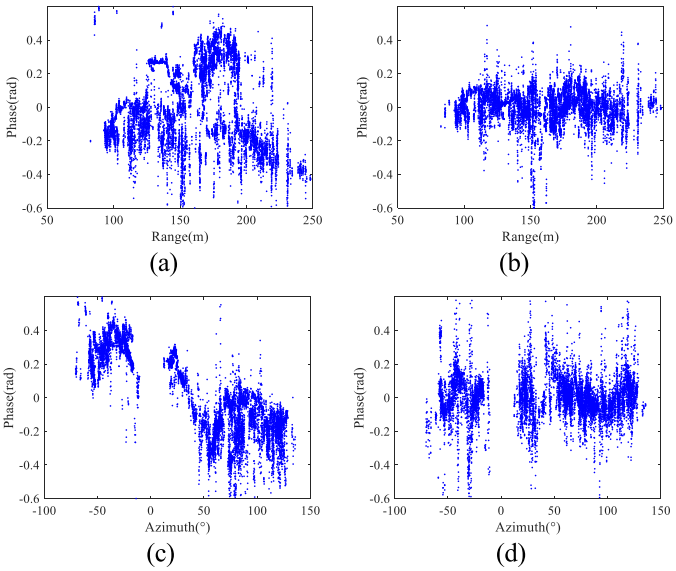

Fig. 18. Compensated phase distribution. (a) Over slant range with model A. (b) Over slant range with model B. (c) Over azimuth angle with model A. (d) Over azimuth angle with model B.

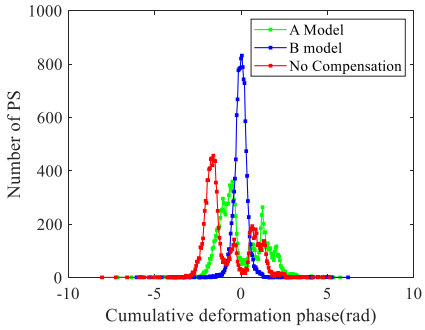

Fig. 19. Cumulative deformation phase distribution curves with different models.

be noted that when using the A model, the estimated phase distribution has a large difference from the interferometric phase distribution. When considering the offset of the rotation center, the estimated phase agrees much better with the interferometric phase.

Fig. 18 shows the phase diagram of the 2nd image with or without compensation using the rotation center offset model. The results after compensation are distributed around 0 rad.

Fig. 19 shows the cumulative deformation phase distribution curve after compensation. Fig. 20 shows the cumulative deformation phase diagram using the A and B models. When the rotation center offset error is not compensated, a large number of PSs retain phase components that change along the azimuth. After removal, the remaining phases are basically distributed around 0 rad. It can be noted that the proposed method can effectively compensate the scanning error phase in differential interferometry.

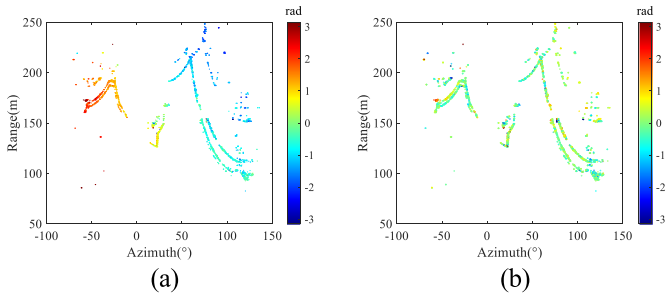

Fig. 20. Accumulated deformation phase after compensation. (a) Model A. (b) Model B.

V. Conclusion

In GB-ArcSAR differential interferometry, the mechanical rotation might cause the rotation center to shift, which affects the deformation measurement accuracy. This article establishes a rotation center offset error model based on the radar imaging geometry. Based on the multivariate Taylor expansion, the functional relationship between the error model and the scene terrain is obtained, which illustrates the influence of different error components on the interferometric phase. A differential interferometry error compensation method based on the PS technology is proposed. This method uses the least squares method to estimate and jointly compensate for the rotation center offset error and the atmospheric disturbance phase. Through the CR and actual scene experiments, the effectiveness of this method is verified.

References

[1] Y. Wang et al., "Ground-based differential interferometry SAR: A review," *IEEE Geosci. Remote Sens. Mag.*, vol. 8, no. 1, pp. 43–70, Mar. 2020, doi: 10.1109/MGRS.2019.2963169.

[2] M. Pieraccini and L. Miccinesi, "Ground-based radar Interferometry: A bibliographic review," *Remote Sens.*, vol. 11, no. 9, Apr. 2019, Art. no. 1029, doi: 10.3390/rs11091029.

[3] R. Iglesias et al., "Ground-based polarimetric SAR interferometry for the monitoring of terrain displacement phenomena–Part II: Applications," *IEEE J. Sel. Topics Appl. Earth Observ. Remote Sens.*, vol. 8, no. 3, pp. 994–1007, Mar. 2015, doi: 10.1109/JSTARS.2014.2366711.

[4] Y. D. C.Hu and W. Tian, "Multistatic ground-based differential interferometric MIMO radar for 3D deformation measurement," *Sci. China Inf. Sci.*, vol. 64, no. 12, Nov. 2021, Art. no. 227301, doi: 10.1007/s11432-021-3352-y.

[5] C. Colesanti and J. Wasowski, "Investigating landslides with space-borne synthetic aperture radar (SAR) interferometry," *Eng. Geol.*, vol. 88, no. 3-4, pp. 173–199, Nov. 2006, doi: 10.1016/j.enggeo.2006.09.013.

[6] F. Viviani, A. Michelini, L. Mayer, and F. Conni, "IBIS-ArcSAR: An innovative ground-based SAR system for slope monitoring," in *Proc. IEEE Int. Geosci. Remote Sens. Symp.*, 2018, pp. 1348–1351, doi: 10.1109/IGARSS.2018.8517702.

[7] Y. Luo, H. Song, R. Wang, Y. Deng, F. Zhao, and Z. Xu, "Arc FMCW SAR and applications in ground monitoring," *IEEE Trans. Geosci. Remote Sens.*, vol. 52, no. 9, pp. 5989–5998, Sep. 2014, doi: 10.1109/TGRS.2014.2325905.

[8] D. Tarchi, H. Rudolf, G. Luzi, L. Chiarantini, P. Coppo, and A. J. Sieber, "SAR interferometry for structural changes detection: A demonstration test on a dam," in *Proc. IEEE Int. Geosci. Remote Sens. Symp.*, 1999, vol. 3, pp. 1522–1524 doi: 10.1109/IGARSS.1999.772006.

[9] S. Rödelsperger, L. Gwendolyn, G. Carl, and M. Becker, "Monitoring of displacements with ground-based microwave interferometry: IBIS-S and IBIS-L," *J. Appl. Geodesy*, vol. 4, no. 1, 2010, pp. 41–54, doi: 10.1515/jag.2010.005.

[10] R. Zhou et al., "A compact MIMO automotive radar using phase-aligned daisy-chain cascading topology and elevation compensation for 2D angle estimation," *Sci. China Inf. Sci.*, vol. 66, no. 6, May 2023, Art. no. 162305, doi: 10.1007/s11432-022-3613-6.
[11] H. Lee, S.-J. Cho, and K.-E. Kim, "A ground-based arc-scanning synthetic aperture radar (ArcSAR) system and focusing algorithms," in *Proc. IEEE Int. Geosci. Remote Sens. Symp.*, 2010, pp. 3490–3493, doi: 10.1109/IGARSS.2010.5652569.
[12] C. Hu, Y. Deng, W. Tian, and T. Zeng, "A compensation method of nonlinear atmospheric phase applied for GB-InSAR images," *J. Radars*, vol. 8, no. 6, pp. 831–840, Dec. 2019, doi: 10.12000/JR19073.
[13] C. Hu, M. Zhu, T. Zeng, W. Tian, and C. Mao, "High-precision deformation monitoring algorithm for GBSAR system: Rail determination phase error compensation," *Sci. China Inf. Sci.*, vol. 59, no. 8, Feb. 2016, Art. no. 082307, doi: 10.1007/s11432-015-5446-z.
[14] Y. Mo, T. Lai, Q. Wang, and H. Huang, "Modeling and compensation for repositioning error in discontinuous GBSAR monitoring," *IEEE Geosci. Remote Sens. Lett.*, vol. 20, Oct. 2023, Art. no. 4012705, doi: 10.1109/LGRS.2023.3323978.
[15] Z. Wang, Z. Li, and J. Mills, "Modelling of instrument repositioning errors in discontinuous multi-campaign ground-based SAR (MC-GBSAR) deformation monitoring," *ISPRS J. Photogrammetry Remote Sens.*, vol. 157, pp. 26–40, Nov. 2019, doi: 10.1016/j.isprsjprs.2019.08.019.
[16] O. Monserrat, M. Crosetto, and G. Luzi, "A review of ground-based SAR interferometry for deformation measurement," *ISPRS J. Photogrammetry Remote Sens.*, vol. 93, pp. 40–48, May 2014, doi: 10.1016/j.isprsjprs.2014.04.001.
[17] H. Lee, J.-H. Lee, K.-E. Kim, N.-H. Sung, and S.-J. Cho, "Development of a truck-mounted arc-scanning synthetic aperture radar," *IEEE Trans. Geosci. Remote Sens.*, vol. 52, no. 5, pp. 2773–2779, May 2014, doi: 10.1109/TGRS.2013.2265700.
[18] B. Osmanoğlu, F. Sunar, S. Wdowinski, and E. Cabral-Cano, "Time series analysis of InSAR data: Methods and trends," *ISPRS J. Photogrammetry Remote Sens.*, vol. 115, pp. 90–102, May 2016.
[19] Y. Izumi, G. Nico, and M. Sato, "Time-series clustering methodology for estimating atmospheric phase screen in ground-based InSAR data," *IEEE Trans. Geosci. Remote Sens.*, vol. 60, 2022, Art. no. 5206309, doi: 10.1109/TGRS.2021.3072037.
[20] X. Zhao, H. Lan, L. Li, Y. Zhang, and C. Zhou, "A multiple-regression model considering deformation information for atmospheric phase screen compensation in ground-based SAR," *IEEE Trans. Geosci. Remote Sens.*, vol. 58, no. 2, pp. 777–789, Feb. 2020, doi: 10.1109/TGRS.2019.2940463.
[21] Y. Deng, C. Hu, W. Tian, and Z. Zhao, "A grid partition method for atmospheric phase compensation in GB-SAR," *IEEE Trans. Geosci. Remote Sens.*, vol. 60, May 2022, Art. no. 5206713, doi: 10.1109/TGRS.2021.3074161.

Yunkai Deng was born in 1992. He received the B.S. and Ph.D. degrees in information and communication engineering from Beijing Institute of Technology, Beijing, China, in 2014 and 2020, respectively.

He is an Assistant Professor and working with Radar Technology Research Institute, Beijing Institute of Technology. His research interests include SAR image processing and DInSAR technology.

Hanpu Zhou was born in 2000. She received the B.S. degree in communication engineering from Hunan University, Changsha, China, in 2022. She is currently working toward the M.S. degree with the Radar Technology Research Institute, Beijing Institute of Technology, Beijing, China, in 2023.

Her research interests include SAR imaging and interferometry.

Weiming Tian was born in 1983. He received the B.S. and Ph.D. degrees in information and communication engineering from the Beijing Institute of Technology, Beijing, China, in 2005 and 2010, respectively.

He is currently working with the Radar Technology Research Institute, Beijing Institute of Technology. His research interests include synthetic aperture radar (SAR) system design and signal processing, bistatic SAR synchronization, and differential interferometric SAR technology.

Xin Xie was born in 1996. He received the B.S. degree in communication engineering from Zhengzhou University, Zhengzhou, China, in 2019. He is currently working toward the Ph.D. degree with the Radar Technology Research Institute, Beijing Institute of Technology, Beijing, China.

His research interests include SAR imaging and interferometry.

Wenyu Li was born in 1999. She received the B.S. degree in electronic information engineering from the Huazhong University of Science and Technology, Wuhan, China, in 2021. She is currently working toward the M.S. degree with the Radar Technology Research Institute, Beijing Institute of Technology, Beijing, China.

Her research interests include radar signal processing and biomedical radar systems.

Cheng Hu was born in Hunan Province, China. He received the B.S. degree in electronic engineering from the National University of Defense Technology, Changsha, China, in 2003, and the Ph.D. degree in target detection and recognition from the Beijing Institute of Technology (BIT), Beijing, China, in 2009.

From 2006 to 2007, he was a Research Associate with the Microwave Integrate System Laboratory, University of Birmingham, Birmingham, U.K. Since 2012, he has been an Associate Professor with the School of Information and Electronics, BIT. His research interests include the geosynchronous SAR, bistatic SAR imaging processing, and forward scatter-radar signal processing.